Gravitational Wave Detection with Photometric Surveys

Yijun Wang,[1,*] Kris Pardo,[2,†] Tzu-Ching Chang,[2,1,‡] and Olivier Doré[2,1,§]

[1] *California Institute of Technology, Pasadena, CA 91125, USA*

[2] *Jet Propulsion Laboratory, California Institute of Technology, Pasadena, CA 91101, USA*

(Dated: October 7, 2020)

Gravitational wave (GW) detections have considerably enriched our understanding of the universe. To date, all the known events were observed via direct detection. In this paper, we study a GW detection technique based on astrometric observation and demonstrate that it offers a highly flexible frequency range that can uniquely complement existing detection methods. Using repeated point-source astrometric measurements, periodic GW-induced deflections can be extracted and wave parameters inferred. We illustrate how high-cadence observations of the galactic bulge, such as offered by the Roman Space Telescope's Exoplanet MicroLensing (EML) survey, have the potential to be a potent GW probe with complementary frequency range to *Gaia*, pulsar timing arrays (PTAs), and the Laser Interferometer Space Antenna (LISA). We calculate that the Roman EML survey is sensitive to GWs with frequencies ranging from 7.7×10^{-8} Hz to 5.6×10^{-4} Hz, which opens up a unique GW observing window for supermassive black hole binaries and their waveform evolution. While the detection threshold assuming the currently expected performance proves too high for detecting individual GWs in light of the expected supermassive black hole binary population distribution, we show that binaries with chirp mass $\mathcal{M}_c > 10^{7.6}\ M_\odot$ out to 10 Mpc can be detected if the telescope is able to achieve an astrometric accuracy of 0.11 mas. To confidently detect binaries with $\mathcal{M}_c > 10^7\ M_\odot$ out to 50 Mpc, a factor of 100 sensitivity improvement is required. We propose several improvement strategies, including recovering the mean astrometric deflection and increasing astrometric accuracy, number of observed stars, field-of-view size, and observational cadence. We also discuss how other existing and planned photometric surveys could contribute to detecting GWs via astrometry.

I. INTRODUCTION

The successful detection of gravitational wave (GW) signals from binary mergers with the Advanced Laser Interferometer Gravitational-wave Observatory (Advanced LIGO) and Virgo collaboration [see e.g. 1, 2] has spurred great interest in improving detection sensitivity and developing independent detection methods. For GW astronomy, it is crucial that we have access to GWs across as wide a frequency spectrum as possible, since different frequency bands are sensitive to their respective groups of GW sources. A continuous frequency band also allows for observation of the same GW source as it evolves to higher frequencies towards merger, allowing us to extract as much information as possible.

The Advanced LIGO is sensitive to GWs between 10 Hz and 7 kHz [3], ideal for detecting solar-mass binary mergers. The deci-hertz band will be covered by space-based detectors such as TianGo [4] and DECIGO [5], targeting intermediate-mass black hole binaries ($\sim 10^2 - 10^4\ M_\odot$ [4]). The milli-hertz band will be covered by the space-based Laser Interferometer Space Antenna (LISA) [6] and TianQin [7]. These interferometer-type detectors directly measure the GW-induced change in separation between either suspended or free falling mirrors. In this case, the detector frequency range is limited by noise factors, such as mirror position alignment error, quantum noise and thermal noise [see, e.g., 8]. The space-based detectors are sensitive to massive black hole mergers (MBHMs) at high redshifts (e.g. LISA can

* yijunw@caltech.edu
† kpardo@caltech.edu
‡ tzu-ching.chang@jpl.nasa.gov
§ olivier.p.dore@jpl.nasa.gov

detect $10^5\ M_\odot$ mergers at $z \sim 15$ with an SNR of ~ 100 in the ringdown stage [6]). Observing MBHMs will be instrumental for modeling black hole evolution history and understanding strong-field gravity features [9].

At lower frequencies, interferometer-type detectors are no longer available and there is a frequency gap until the Pulsar Timing Array (PTA) detection method becomes applicable. PTAs measure the Time of Arrival (TOA) of pulses from stable milli-hertz pulsars. Passing GWs modify the pulse frequency, which translates into a timing residual signal. By cross-correlating timing residuals from pairs of pulsars, GW parameters can be extracted [10–12]. The PTA frequency band is limited by mission lifetime as well as the observational cadence. For example, a 5-year survey with an observational frequency of 17 year^{-1} ($\sim 1/3$ week^{-1}) [13, 14] is sensitive to GWs from 6.3×10^{-9} Hz to 5.4×10^{-7} Hz. With longer signal integration time and more pulsar pairs, PTAs can detect the supermassive black hole merger background (SMBHMB) as well as individual supermassive black hole binaries (SMBHBs) with chirp mass between $10^4\ M_\odot$ and $10^{10}\ M_\odot$ [15].

Aside from direct detection and PTAs, we can also detect GWs via astrometry [16, 17]. Analogous to the theoretical basis for PTAs, passing GWs perturb photon trajectories as they travel from the observed stars to the detector. This perturbation leaves a GW-specific change to the apparent star positions. It is, in principle, possible to extract this change in position from high-precision astrometric data. Similar to the PTA method, the sensitive frequency range depends on both survey lifetime and observational cadence. Accordingly, using astrometric data as GW probes is a highly flexible technique since observational frequency is tunable, depending on mission design. A suitable photometric survey with cadence higher than PTAs can unlock the intermediate frequency band between PTAs and LISA. A survey with such sensitivity range would be able to detect massive black hole binaries from $10^5\ M_\odot$ to $10^9\ M_\odot$ during inspiral and close to merger. Detecting these GW sources will be invaluable for informing black hole evolution models. Accessing this frequency range also opens up opportunities for joint analysis with PTAs and LISA for signals that evolve across the frequency bands. A longer signal containing distinct features from different phases of the merging event thus provides more handle on the GW source property.

This astrometric GW detection method in the context of *Gaia* has been studied in detail [18, 19]. *Gaia* as a GW probe is sensitive from $10^{-8.5}$ Hz to 10^{-6} Hz; at $f > 10^{-7.5}$ Hz, *Gaia* will outperform PTA efforts [19]. In this paper, we discuss how this method can be generalized to photometric surveys, and specifically to the Nancy Grace Roman Space Telescope[1], NASA's next flagship observatory after the James Webb Space Telescope.

The Roman Space Telescope will observe billions of galaxies and thousands of supernovae to probe the time evolution of dark energy and large-scale structure [see, e.g., 20]. It will perform a micro-lensing survey on the inner Milky Way, as well as high contrast imaging and spectroscopic studies of individual close-by exoplanets [21]. For GW detection, its notional Exoplanet MicroLensing (EML) survey is particularly relevant. It is expected to observe 10^8 stars in 7 fields [22]. It operates in the near-IR with a $\sim 0.281\,\mathrm{deg}^2$ field of view (FoV), with an estimated single-exposure astrometric precision of 1.1 mas [23]. During its nominal lifetime of 5 years, it will survey a total area of $1.97\,\mathrm{deg}^2$ between Galactic longitudes of -0.5 deg and 1.5 deg, and Galactic latitudes between -0.5 deg and -2 deg. Observational time consists of six 72-day seasons. During each season, the Roman Space Telescope visits the seven fields sequentially and repeats this cycle every 15 minutes. This gives a maximum of $\sim 41,000$ exposures per source, making it "one of the deepest exposures of the sky ever taken" [22].

In this paper, we begin by reviewing the theory for GW-induced astrometric deflections and

[1] https://roman.gsfc.nasa.gov/

outlining the general strategy for using photometric surveys as GW probes. We then assess the potential of the Roman EML survey to detect individual binary signals. In Section IV, we discuss directions for performance improvement for photometric surveys similar to the Roman EML survey as GW probes. We then expand to other telescopes and surveys and discuss their potential for astrometrically detecting GWs.

All of the code used to produce the figures and analysis in this paper is available at: https://github.com/kpardo/estoiles-public.

II. PHOTOMETRIC SURVEYS AS GW PROBES

In this section, we first summarize how GW signatures manifest as observable variation in the astrometric solution. We then present estimates of the sensitivity of photometric surveys to GWs as well as their frequency resolution.

A. GW Signature in Astrometry

In short, a passing GW perturbs the spacetime along the photon trajectory as it travels from the observed star to the detector. This perturbation causes a shift in the stellar apparent position from its true position. Theoretical details are derived in [17] in the distant source limit and later generalized in [16]. Here we present a brief summary, closely following steps in [16].

We start with the model where the GW source and observer are stationary in Minkowski spacetime and the GW is a linear perturbation to flat spacetime. Throughout this paper, we use Greek alphabet to denote components of 4-vectors and Latin alphabet to denote the spatial dimensions. Indices that appear both as upper and lower indices imply summation over all dimensions. We also adopt the transverse-traceless gauge. Under this gauge condition, components of the perturbation tensor, $h_{\mu\nu}$, can be non-zero only when both indices are spatial, and the tensor trace is 0, i.e.:

$$h_{0\mu} = 0,\ h^{\mu}_{\mu} = 0\ .$$

The metric can then be written as:

$$ds^2 = -dt^2 + (\delta_{ij} + h_{ij})dx^i dx^j\ . \tag{1}$$

We can write the photon trajectory as:

$$x^{\alpha}(\lambda) = x^{\alpha}_{(0)}(\lambda) + x^{\alpha}_{(1)}(\lambda)\ , \tag{2}$$

where subscript (0) indicates quantities in unperturbed spacetime, and subscript (1) indicates first order corrections. λ is the associated affine parameter. We calculate the Christoffel symbols in this metric and write the geodesic equation as:

$$\frac{d^2x^0_{(1)}}{d\lambda^2} = -\frac{\omega_0^2}{2} n^i n^j h_{ij,0} \tag{3}$$

$$\frac{d^2x^k_{(1)}}{d\lambda^2} = -\frac{\omega_0^2}{2}\Big[-2n^i h_{ki,0} + n^i n^j \big(h_{ki,j} + h_{kj,i} - h_{ij,k}\big)\Big]\ , \tag{4}$$

where ω_0 is the photon frequency without GW perturbation. Integrating the geodesic equation with respect to λ gives the photon trajectory and 4-momentum.

We then compute the GW perturbation in the observer frame. We first construct an orthonormal tetrad, $e_{\hat{\alpha}}$ where $e_{\hat{0}} = \vec{u}$ and $\vec{u}$ is the observer's 4-velocity. We also require this tetrad to be parallel-transported along the observer worldline. Imposing the parallel-transport equation and the metric, we can express the observer tetrad in terms of the GW and the unperturbed basis vectors. The observed photon 4-momentum, $k^{\hat{\alpha}}$, can be found via a coordinate transformation, and its spatial part gives $n^{\hat{i}}$. Assuming small deflections, $dn^{\hat{i}} = n^{\hat{i}} - n^{\hat{i}}_{(0)}$.

It is oftentimes useful to assume monochromatic plane-wave GWs and a distant source, in which case the observed star is many GW wavelengths away from the observer. In the plane-wave model, the integral along geodesics can be done analytically, resulting in some geometrical constant factors and a phase in the

form of $e^{-i2\pi f\omega_0(1+\mathbf{p}\cdot\mathbf{n})\lambda_s}$, where $2\pi f$ and ω_0 are frequencies of the GW and the photon, respectively. $\mathbf{p}$ is the GW propagation direction and $\mathbf{n}$ points towards the observed star. In the distant source limit (i.e., $\omega_0\lambda_s \gg c/2\pi f$), prefactors to the integral become negligibly small and we may ignore this term. Consequently, the leading order of the signal depends only on the GW amplitude at the observer. $dn^{\hat{i}}$ is thus much simplified and becomes [16, 17]:

$$dn^{\hat{i}}(t,\mathbf{n}) = \frac{n^i + p^i}{2\,(1+\mathbf{p}\cdot\mathbf{n})} h_{jk}(t,\mathbf{0}) n^j n^k - \frac{1}{2} h^{ij}(t,\mathbf{0}) n_j \ , \tag{5}$$

$$h_{ij}(t,\mathbf{x}) = \mathrm{Re}\left[\mathcal{H}_{ij} e^{-i2\pi f(t-\mathbf{p}\cdot\mathbf{x})}\right] \ , \tag{6}$$

where $\mathcal{H}_{ij}$ denotes the plane wave amplitude tensor. The distant source approximation is also adopted in PTA analyses, where the integral from the pulsar to the observer is reduced to consideration about the two end points only (see, e.g.,[24]). For PTA analyses, an additional reason to drop the GW term at the pulsar is that such a signal would be uncorrelated between different pulsars, whereas the GW perturbation at the detector is shared. When we consider the correlation between timing residuals, these pulsar perturbation terms can thus be treated as random noise [10]. In Section III we discuss the validity of this assumption in our work.

For small astrometric deflections, it suffices to consider the leading order of $\mathcal{H}_{ij}$ [see e.g. 25],

$$\mathcal{H}_{ij} = A H_{ij}(\mathbf{p}) \tag{7}$$

$$A_{(0)} = \frac{2G^{5/3}}{c^4}(\pi f)^{2/3}\frac{\mathcal{M}_c^{5/3}}{D_L} \sim f^{2/3} M_s^{5/3} \ . \tag{8}$$

$H_{ij}(\mathbf{p})$ is the polarization tensor for GWs propagating along $\mathbf{p}$. $A_{(0)}$ is the leading term of the GW amplitude, A, which depends on the source frame GW frequency, f, the chirp mass, $\mathcal{M}_c$, and the luminosity distance, D_L. $\mathcal{M}_c$ is defined as $m\left(q/(1+q)^2\right)^{3/5}$, where m is the total mass of the binary and q is the mass ratio, m_1/m_2, assuming m_1 is the smaller mass. For GW sources not at cosmological distances (i.e., redshift $z \ll 1$), we may ignore the cosmological redshift to the wave frequency. Throughout this paper, we always assume such close-by sources and we do not differentiate between source frame and observer frame GW frequency. Our threshold GW source estimates validate this assumption. To this order, we note that scaling $\mathcal{M}_c$ by an arbitrary factor κ is completely degenerate with scaling D_L by $\kappa^{5/3}$. Therefore, it is convenient to define a scaled mass $M_s \equiv \mathcal{M}_c/D_L^{3/5}$, which represents all sources that give the same leading order GW signal, at a fixed frequency.

In Figure 1 we reproduce Figure 1 in [19] and illustrate the astrometric deflection pattern for a field of stars in the northern hemisphere in Galactic coordinates, due to a face-on GW source at zenith. It is clear that the deflection magnitude is largest on the Galactic plane. Deflections induced by the plus and cross polarizations are orthogonal, and the quadrupolar pattern is clear. The right panels show the astrometric deflection in a square Field of View (FoV), assuming the telescope is in the Galactic plane and points directly to the Galactic center. This FoV model has roughly the same area as the true FoV of the Roman Space Telescope but differs in shape. We adopt it nonetheless in our analysis for simplicity. The bottom panel shows the total deflection pattern while the upper panel shows the deflection pattern after subtracting the mean deflection. This is expected to be the actual observed signal, as the pointing reconstruction strategy of the Roman Space Telescope will likely absorb deflections uniform across the FoV; for further discussions see Section IV.

The magnitude of the astrometric deflection as a function of the GW source position on the sky is shown in Figure 2. We assume the telescope FoV points to the Galactic center. Properties of this GW source are the same as in Figure 1. For illustration purpose, we fix the polarization angle to be 0. The mean deflection is averaged over 1000 randomly distributed

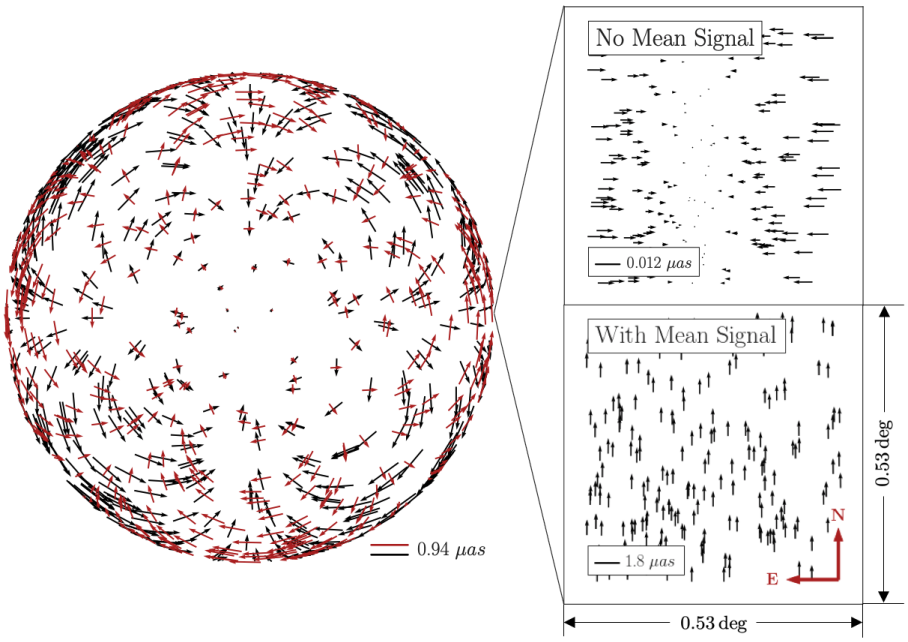

FIG. 1. Illustration of the expected stellar astrometric deflections. *Left:* Orthographically projected dn for a subset of stars observed by *Gaia* in the northern hemisphere onto the galactic plane [inspired by a very similar plot in 19]. The North Galactic pole is at the center which is also the position of the GW source. Black arrows correspond to the real part of the waveform at GW phase $\phi = 0$ (plus polarization), and the red arrows correspond to that at $\phi = \pi/4$ (cross polarization). The source is a 10^9 $M_\odot$ equal-mass binary black hole at 1 Mpc at $(l = 90\,\mathrm{deg}, b = 90\,\mathrm{deg})$ in galactic coordinates, emitting GWs at 10^{-6} Hz. This inclination angle is set to $i = 0$ (i.e. face-on) and the polarization angle is $\psi = 0$. *Right:* Deflections within the Roman Space Telescope's FOV during the EML survey. The lower panel shows the total deflection, and the upper panel shows the deflection after subtracting the mean, since the mean is expected to be absorbed in the pointing reconstruction; for further discussion see Section IV. Star coordinates are selected from the Gaia Data Release 2 catalog, with brightness $0 < G < 9$ [26, 27]. Density of stars reflects only a subset of the true stellar density in the catalog.

stars within the FoV (the number of stars is not representative of the actual stellar density; it is picked for clear visualization) The deflection is maximal when the GW source position is orthogonal to observed star positions, which is consistent with Equation 5 and Figure 1.

B. Sensitivity Curve Estimate

For single exposures, the astrometric accuracy, $\Delta\theta$, is determined by pixel size and pixel placement error [23]. Typically, astrometric deflections due to GWs are small compared to any realistic single-exposure resolution values, therefore they cannot be resolved from isolated measurements of individual stars. This limit, however, can be statistically improved by considering repeated observation of a vast collection of stars.

Firstly, within each exposure, we consider the correlated astrometric deflection between N_s stars, which improves the resolution by $\sqrt{N_s}$. Secondly, we note that the GW-induced deflections are periodic in time. If we schedule the

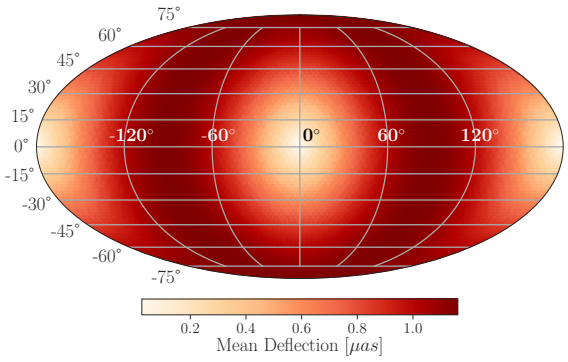

FIG. 2. Mean maximal deflection due to GW sources at different Galactic coordinates. The FoV is fixed to point towards the Galactic center, i.e. $l = 0\,\mathrm{deg}$, $b = 0\,\mathrm{deg}$. The magnitude is calculated as that of the orthographic projection of dn in the FoV, averaged over all observed stars. The maximum occurs when the source position vector is perpendicular to the star position vectors, which is consistent with Equation 5. Aside from its coordinates, the GW source at each position has the same properties as that in Figure 1.

telescope to visit the same field multiple times, we can capture N_c cycles of this oscillatory deflection pattern. More observed cycles give us a better handle on the pattern, which improves sensitivity by $\sqrt{N_c} = \sqrt{T_{\rm obs} f}$, where $T_{\rm obs}$ is the total observation time and f is the GW frequency or, identically, deflection pattern oscillation frequency. The minimum detectable characteristic strain amplitude is then

$$h_c = \sqrt{\frac{3}{2\pi^2}} \frac{\Delta\theta}{\sqrt{N_s N_c}} \sim \frac{\Delta\theta}{\sqrt{N_s T_{\rm obs} f}} \tag{9}$$

where the numerical prefactor depends on conventions that relate characteristic strain amplitude and the GW energy density [16, 28, 29]. These two statistical improvements are subject to survey-specific constraints. In Section III, we provide further discussion on this limit in the context of the Roman EML survey. Throughout our analysis, we assume that, within certain limits, high frequency oscillations are sampled equally well as low frequency ones, i.e. without including discrete sampling effects. In reality, the discrete telescope schedule to visit a sky patch and mission duty cycle impose an upper limit on the maximum number of observable cycles, i.e., the GW frequency, before the deflections become poorly sampled.

C. Frequency Resolution

In this subsection, we outline how to calculate the GW frequency resolution of a photometric survey. From the instrument perspective, the frequency resolution is determined by the exposure timing accuracy, σ_t. To calculate how σ_t translates into end-of-mission frequency resolution, Δf, we model the registered time of the j-th observation as a quadratic function

$$\begin{aligned} t_j &= t_0 + \left.\frac{dt}{dN}\right|_j N_j + \frac{1}{2}\left.\frac{d^2t}{dN^2}\right|_j N_j^2 \\ &\equiv t_0 + a_1 N_j + a_2 N_j^2 \,, \end{aligned} \tag{10}$$

where N_j is the number of observed cycles at time t_j. By definition,

$$a_1 = \frac{dt}{dN} = \frac{1}{dN/dt} = \frac{1}{f} \tag{11}$$

$$2a_2 = \frac{d^2t}{dN^2} = -\frac{\dot{f}}{f^3} \,, \tag{12}$$

evaluated at $N_j = 0$. We then use the Fisher information matrix to calculate the variance of the quadratic coefficients, a_1, a_2, which we use to further calculate variance of frequency and change of frequency, $\sigma_f, \sigma_{\dot{f}}$. $\sigma_{a_1}, \sigma_{a_2}$ are given by

$$\sigma_{a_1} \sim \frac{\sigma_t}{N^{3/2}}, \;\; \sigma_{a_2} \sim \frac{\sigma_t}{N^{5/2}} \,. \tag{13}$$

We note that, to leading order, $N = T_{\rm obs} f$. For the second order correction, we may also treat the first order correction coefficient, a_1, or, equivalently, f, as constant. We therefore get

$$\sigma_{\dot{f}} \sim f^3 \sigma_{a_2} \sim f^{1/2} \frac{\sigma_t}{T^{5/2}} \,. \tag{14}$$

The campaign frequency sensitivity is then estimated by

$$\Delta f = \sigma_f T_{\rm obs} \ . \tag{15}$$

To determine whether this resolution is sufficient to capture frequency change of GWs within the detector frequency band, we compare Δf with the frequency evolution of observable sources. The intrinsic inspiral binary frequency is given by [see, e.g., 30]

$$f \sim \frac{1}{m\pi}\left(\frac{1}{4\eta^{1/4}}\left(1+\eta_1\Theta^{-1/4}\right)\right)^{3/2} \ , \tag{16}$$

where $\eta \equiv q/(1+q)^2$ and m and q are the total mass of the binary (in natural units where $G = c = 1$) and the mass ratio, as defined before. η_1 is defined as $743/4032 + 11/48\eta$ and Θ as $\eta\,(t_c - t)\,/5m$. Time to coalesce t_c is $5m/\left[\eta\,(8\pi m f)^{8/3}\right]$. For systems that remain in inspiral stage throughout survey time, we consider the difference of GW frequencies evaluated at the beginning and the end of the survey. For systems that merger within observational time, we take the final frequency to be the Innermost Stable Circular Orbit frequency, $f_{\rm ISCO}$, beyond which the systems quickly coalesce and Equation 16 no longer captures the actual frequency.

This characteristic frequency progression could help distinguishing the GW signal from other noise factors and provide additional information for GW source parameter estimation.

III. DETECTING GWS WITH THE ROMAN SPACE TELESCOPE

In this section, we explore the potential of the Roman EML survey as a GW probe. We first discuss its sensitivity frequency range following the method outlined in Section II. Since the procedure is general, we apply a parallel analysis on *Gaia* for comparison. We then describe a method to extract GW signals from photometric data via Bayesian inference. We apply this technique to the Roman Space Telescope and calculate its sensitivity curve.

A. Roman EML Survey Sensitivity Curve

Similarly to PTAs, the GW frequency band of photometric surveys is constrained by the observation time span and cadence. At the low frequency limit, the GW period should not be longer than the observation time. Signals with longer period are close to being linear over the observational window and thus are likely to be absorbed as telescope motion or proper motion in the astrometric solution. At the high frequency limit, the GW period should not be shorter than twice the observational cadence to satisfy the Nyquist-Shannon sampling condition.

In addition, the low frequency limit is subject to more detailed and survey-specific modifications. Firstly, the low frequency limit where $f_{\rm min} \approx 1/T_{\rm obs}$ can be technically relaxed to $f_{\rm min} \approx 1/2T_{\rm obs}$, since the former limit still produces an oscillatory signal that cannot be fully absorbed by any linear proper motion model [18]. However, we note that this only leads to a factor of two difference, and we ignore this factor when estimating the frequency range. Furthermore, the general guideline works best for uniform sampling, whereas actual surveys may have significant periods of downtime between observational windows. In this case, detecting low frequency GWs requires precisely piecing together high-cadence observation seasons that may be quite separated in time. Deflection change within each season is only a fraction of the total amplitude, and may well be approximated by linear proper motion. Considering the magnitude of the signal and uncertainties from long season-separation, this wave reconstruction process will likely introduce large errors that render further data analysis unfeasible. For a conservative limit, $f_{\rm min}$ is $1/2T_s$ where T_s is the length of one observational season.

Specifically for the Roman EML survey, we assume a 15-minute cadence with six 72-day observational seasons spread out over the nominal 5-year mission time. The previous constraints

then give a conservative frequency range as:

$$7.7 \times 10^{-8}\ \text{Hz} < \Omega_{\text{Roman}} < 5.6 \times 10^{-4}\ \text{Hz}\ .$$

We also assume a single-exposure astrometric accuracy of $\Delta\theta \sim 1.1$ mas, estimated for $H_{AB} = 21.6$ stars, [23] and a total of $N_s \sim 10^8$ stars with $W145_{AB} < 23$ [22]. We note that all GW signals within the Roman EML survey frequency range have wavelengths smaller than ~ 0.1 pc, which is much smaller than the distance to any stars Roman Space Telescope observes. Therefore we may safely use the distant source limit described in Section II.

We now calculate the frequency resolution, following the procedure in Section II. Taking a conservative timing accuracy of 1 s and $T_{\text{obs}} = 6 \times 72$ days (i.e., assuming all seasons happen consecutively), we estimate Δf to be $\sim 10^{-14}$ Hz and $\sim 10^{-12}$ Hz for signals at the lower and upper frequency band limit, respectively. For light systems ($\log_{10} \mathcal{M}_c[M_\odot] = 5.7$), intrinsic frequency change of GWs during the inspiral ranges from 10^{-11} Hz to 10^{-2} Hz, depending on its frequency at the start of the observation. If such a system is initially observed to emit GW at $\sim 6 \times 10^{-5}$ Hz or higher, it coalesces within T_{obs}. For heavy systems ($\log_{10} \mathcal{M}_c[M_\odot] = 9.7$), GW frequency change ranges from 10^{-8} Hz to 10^{-6} Hz. Such heavy systems coalesce within the observational time window if they emit GW at $\sim 2 \times 10^{-7}$ Hz at the start of the mission. In all cases, the Roman EML survey will be sensitive to the frequency evolution of detected GWs. We note that it should increase the sensitivity of the Roman EML survey to GWs; however, a full analysis of this effect is outside the scope of this work.

For *Gaia*, assuming 70 evenly-spaced visits of the same stars, uniformly spread out over the nominal 5-year mission time [26], the frequency range is:

$$6.3 \times 10^{-9}\ \text{Hz} < \Omega_{Gaia} < 4.5 \times 10^{-7}\ \text{Hz}\ .$$

This range differs from [18] at the upper limit, since they used the *Gaia* rotational period of $\sim$ 6h as the cadence. Since we are interested in the average sensitivity applicable to the majority of the observed stars, we adopt the more conservative cadence of 70/5-year. We adopt $\Delta\theta \sim 0.7$ mas, which is the parallax uncertainty for $G \sim 20$ stars in *Gaia* Data Release 2 [31]. This magnitude threshold value is picked for convenient comparison with the Roman EML survey, where relatively fainter stars could also be observed in the near IR. We assume $N_s \sim 10^9$ [27].

Applying Equation 9 to the frequency range of the Roman EML survey and *Gaia*, we compute their strain sensitivity curves, respectively shown as solid black line and dot-dashed line in Figure 3. Sensitivity curves for the International Pulsar Timing Array (IPTA) [see 13, 14] and LISA [32] are shown for comparison as dotted and dashed lines. In anticipation of the GW sources we hope to detect with the Roman EML survey, we display with shaded area the maximal possible characteristic strain amplitude for sources at a luminosity distance of $D_L = 10$ Mpc with a mass ratio $q = 1$ [25, 28] in the range of the Roman EML survey.

The characteristic strain amplitude segment at the lower frequency end in the Roman EML survey range follows the $-1/6$ power law, since the frequency domain inspiral GW strain amplitude follows the -7/6 power law [33], and $h_c \equiv 2fh$ [10]. In this range, we set the chirp mass to be $10^{9.7}\ M_\odot$, the most massive systems we consider in our study. Near 10^{-6} Hz, $10^{9.7}\ M_\odot$ binaries reach the ISCO. Beyond this frequency, these binaries quickly coalesce and Equation 8 no longer captures the actual GW waveform. We do not consider these binaries throughout this study.

For comparison, we also plot the supermassive black hole binary background strain [15] in the IPTA frequency band, and massive black hole merger strain at $z = 3$ in the LISA band from 3×10^{-4} Hz to 1×10^{-2} Hz. For the merger signal in the LISA band, the binaries are the most massive ones that have yet to reach the ISCO at each frequency.

Due to having fewer observed stars, the Roman EML survey has slightly worse sensitivity than *Gaia* at overlapping frequencies. However, its significantly higher cadence allows for the detection of 10^{-6} Hz $- 10^{-5}$ Hz GWs, which are

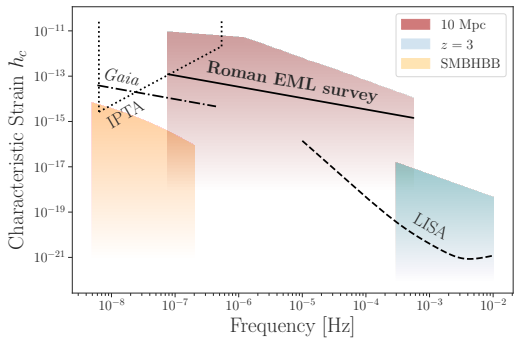

FIG. 3. Strain sensitivity illustration of various GW detectors and example signals. Sensitivity curves for the Roman EML Survey, *Gaia*, LISA and IPTA are given by the solid, dotted-dashed, dashed and dotted lines (the high-frequency end of the LISA frequency band is not shown). The blue and red blocks marks the maximal characteristic strain from equal-mass black hole binary inspirals at 10 Mpc and $z = 3$ (~ 13 Gpc). The yellow block marks the expected strain from the supermassive black hole binary background (SMBHBB). Sensitivity curves for *Gaia* and the Roman EML Survey assume the mean deflection signal is observable. As is shown, the frequency band from roughly 5×10^{-7} Hz to 1×10^{-5} Hz is uniquely accessed by Roman EML.

inaccessible by other dedicated GW observatories such as PTAs and LISA. Specifically, SMBHBs with $\mathcal{M}_c \sim 10^8\ M_\odot - 10^9\ M_\odot$ merge in this frequency range. The larger strain amplitude and faster frequency evolution make them easier to detect than during the inspiral stage in the PTA band. At the high frequency range, $\mathcal{M}_c \sim 10^5\ M_\odot$ massive black hole binaries are at the inspiral stage. Such systems coalesce in the LISA band and would appear as short burst signals. For binaries with masses in between, their inspiral and merger stages could be observable within this frequency range, offering invaluable data to constrain models on massive black hole evolution.

B. Parameter Estimation Strategy

GW signals in astrometric measurements can be extracted via Bayesian inference. This analysis framework is demonstrated in [19], where the authors implement a signal injection-retrieval study tailored for *Gaia*. Specifically, they consider a set of mock *Gaia* exposures and obtain posterior distributions for seven GW source parameters, plus and cross polarization amplitudes, $h_{+,\times}$, their respective initial phases, $\phi_{+,\times}$, GW frequency, f and two angles describing direction to the GW source, $\vec{q}$ (equivalent to $-\mathbf{p}$ in Section II). In this paper, we focus on characterizing the intrinsic binary parameters that are detectable from the Roman EML survey data. For this purpose, we fix the extrinsic parameters (i.e., GW phase, polarization angle and source position) and derive limits on the binary chirp mass, $\mathcal{M}_c$, and luminosity distance, D_L, across the Roman EML survey frequency spectrum. Specifically, we set the wave phase, inclination angle, and polarization angle to 0. We also fix the GW source at the zenith position in the Galactic frame, as illustrated in Figure 1. Fixing the contribution from phase and positional parameters, either by assigning specific representative values, as we do, or by numerically and analytically marginalizing over them, is also commonly adopted in PTA studies to reduce search space dimensions [see, e.g., 10–12].

Under our assumption, we consider the optimal case for detection. As the relative angle between the star position, $\mathbf{n}$, and the GW source position, $\vec{q}$, decreases, signal magnitude decreases accordingly and the detection threshold becomes more stringent. By fixing the GW phase to be 0, we simulate the *a posteriori* analysis, where, after observing at least one deflection cycle, we can determine the deflection amplitude from the entire data set.

We now outline the analysis procedure, closely following the steps in [19]. We start by modeling the observed position of star I at time J, $\vec{s}_{I,J}$, as

$$\vec{s}_{I,J} = \vec{n}_{I,J} + \vec{r}_{I,J} + d\vec{n}_{\mathrm{GW,I,J}}\ , \qquad (17)$$

where $\vec{n}_{I,J}$ is the true position, $\vec{r}_{I,J}$ is random noise and $d\vec{n}_{\rm GW,I,J}$ is the GW-induced deflection, with components given by Equation 5. The true position, $\vec{n}_{I,J}$, can be modeled as a quadratic function in time:

$$\vec{n}_{I,J} = \vec{n}_{I,J'} + \vec{b}_1(t_J - t_{J'}) + \frac{1}{2}\vec{b}_2(t_J - t_{J'})^2 \ , \quad (18)$$

where $\vec{n}_{I,J'}$ is the true position of star I at a reference epoch J' near J. $\vec{b}_{1,2}$ represent proper motion due to stellar velocity and acceleration, evaluated at J'. We can determine these coefficients by extrapolating proper motion measurements from other surveys (e.g. *Gaia*) and modeling the galactic potential. $\vec{n}_{I,J}$ is then subtracted from $\vec{s}_{I,J}$, and the signal residual is random noise plus potential GW signals. The noise is modeled as a zero-mean Gaussian distribution with the standard deviation equal to the single-exposure astrometric accuracy, σ. Noise is assumed to be uncorrelated between stars and different exposures.

The signal after subtracting proper motion is then

$$\begin{aligned} d\vec{s}_{I,J} &\equiv \vec{s}_{I,J} - \vec{n}_{I,J} \\ &= \vec{r}_{I,J} + d\vec{n}_{\rm GW,I,J} \ . \end{aligned} \quad (19)$$

Although this should be our observational data in theory, we most likely will not have the full deflection signal available in the residual of an astrometric solution. For a typical photometric survey, any deflection shared by all stars within the FoV is likely to be absorbed when the telescope pointing solution is calibrated to obtain absolute astrometry. Therefore, we subtract the mean deflection of all stars and adopt the mean-free residual as our signal for analysis. Since the Roman Space Telescope FoV is small compared with the typical variation scale of GW-induced deflection pattern (see Figure 1), the mean-free signal is much smaller in magnitude than $d\vec{n}_{\rm GW,I,J}$, imposing a more demanding detection threshold. In Section IV, we provide details on how absolute astrometric solution can be recovered from Roman Space Telescope data and investigate its effects on our result. The signal is then:

$$\delta\vec{n}_{\rm GW,I,J} = d\vec{s}_{I,J} - \frac{1}{K}\sum_{I=1}^{K} d\vec{n}_{\rm GW,I,J} \ , \quad (20)$$

where K is the total number of stars within the FoV. The likelihood function of a particular GW model at the exposure labeled by J is then given by:

$$\begin{aligned} &P\left(d\vec{s}_J|\Psi\right) \\ &\propto \exp\left(-\frac{1}{2}\sum_{I=1}^{K}\frac{\left(d\vec{s}_{I,J} - \delta\vec{n}_{\rm GW,I,J}(\Psi)\right)^2}{\sigma^2}\right) \ , \end{aligned} \quad (21)$$

where Ψ represents GW source parameters.

By fixing the positional angles and phase, we focus on the intrinsic parameters of the GW source, i.e., wave amplitudes, $A_{+,\times}$. Since we expect the signal to be small, any higher order correction will be overwhelmed by noise, and it suffices to consider the leading order contribution in Equation 8, which depends only on the scaled mass M_s.

We perform this Bayesian analysis on one exposure only (i.e. summing over I but not J), where the stellar astrometric deflection is maximal, i.e., at one of the GW peaks, by tuning and fixing the GW phase. We do not model all other exposures during the mission lifetime; instead, we estimate the effect of including them in our analysis by scaling down the astrometric accuracy by $\sqrt{N_c}$ where N_c is the expected number of observed deflection cycles as in Equation 9.

To determine the detection thresholds, we run Markov chain Monte Carlo (MCMC) simulations using the Python package `emcee` with no injection signal and determine the $68\%, 95\%$ and 99.7% upper limits on M_s. The FoV is modeled as a 0.53 deg $\times$0.53 deg square centered on the galactic center.

For computational efficiency, we randomly populate the FoV with 1000 stars. To account for the effect of the expected 10^8 observed stars, we scale down σ by $\sqrt{10^5}$. We adopt a flat prior between:

$$4.54 < \log_{10} M_s \ [M_\odot/{\rm Mpc}^{3/5}] < 11.54 \ ,$$

which is equivalent to flat priors between:

$$5.74 < \log_{10} \mathcal{M}_c \ [M_\odot] < 9.74$$

and

$$-3 < \log_{10} D_L \ [\mathrm{Mpc}] < 2 \ .$$

The upper bound of chirp mass is chosen such that the GW sources are realistic and have significant lifetime within the frequency band of the Roman EML survey. Priors on the luminosity distance and the lower bound on chirp mass are chosen to produce sufficiently strong signals in light of the theoretically calculated sensitivity curve.

The detectable $\log_{10} \mathcal{M}_c - \log_{10} D_L$ parameter space at selected GW frequencies is show in Figure 4. In the left column, for example, we show that at $f = 1 \times 10^{-6}$ Hz, a chirp mass 10^9 $M_\odot$ massive black hole binary at 1 Mpc can be detected with 95% confidence level (2σ). Example posterior distributions are shown for the same binary system at different D_L. Systems that already reach the ISCO are excluded from the accessible parameter space, since they quickly coalesce afterwards, and our analytical waveform expression in Equation 8 for the inspiral stage no longer captures the actual GW waveform. Specifically, [see, e.g., 34]

$$f_{\mathrm{ISCO}} = \frac{c^3}{6^{3/2}\pi G} \frac{(q^2(1+q))^{3/10}}{\mathcal{M}_c} \ , \qquad (22)$$

and

$$\mathcal{M}_c(f)_{\max} = \frac{c^3}{6^{3/2}\pi G} \frac{2^{3/10}}{f} \ , \qquad (23)$$

where, since $\mathcal{M}_c(f)_{\max}$ is an increasing function of q, we set $q = 1$. Figure. 4 shows that, at all frequencies, the detectable parameter space is reduced significantly by subtracting the mean signal, and for GW with frequencies larger than 1×10^{-6} Hz, the parameter space is increasingly affected by the ISCO limit.

We summarize in Figure 5 the detection threshold across the Roman EML survey frequency band by plotting the 95% upper limit on $\mathcal{M}_c$ at 100 kpc and 1 Mpc. Detection thresholds assuming an astrometric accuracy of 0.11 mas or full astrometric deflection signal are also plotted. As expected, the range of the detectable GW sources is limited by the signal strength and intrinsic frequency limits. Between these two competing factors, the "sweet spot" frequency with the largest accessible parameter space in the $\log_{10} \mathcal{M}_c - \log_{10} D_L$ plane is roughly located at 10^{-6} Hz. With its current expected performance, the Roman EML survey is sensitive to GWs from massive black hole binaries with $\mathcal{M}_c > 10^{7.8}$ $M_\odot$ up to $D_L \sim 1$ Mpc. Although this threshold excludes many of the interesting GW sources we hope to detect, Figure 5 shows that such sources out to 10 Mpc could be observable if the Roman Space Telescope can achieve a 0.11 mas astrometric accuracy, which is a possible improvement over the currently estimated 1.1 mas.

IV. DISCUSSION

In this section, we elaborate on the Roman Space Telescope pointing reconstruction strategy and evaluate its impact on GW detection. We then propose recommendations for maximizing the seredipitous GW scientific output from photometric survey instruments. Finally, we review some ongoing and planned surveys and discuss their merits and drawbacks as potential GW probes.

A. Roman Space Telescope Pointing Reconstruction and GS Selection

Here we expand on the mean subtraction technique discussed in Section III and assess its impact on the reach of the Roman EML survey as a GW probe.

Prior to launch, 4 to 18 guiding stars (GSs) will be selected in each observed field [23]. Of the 18 detectors of the Roman Space Telescope, each contains at most one guiding star. These stars are likely to be bright, and their precise absolute positions and proper motion will be

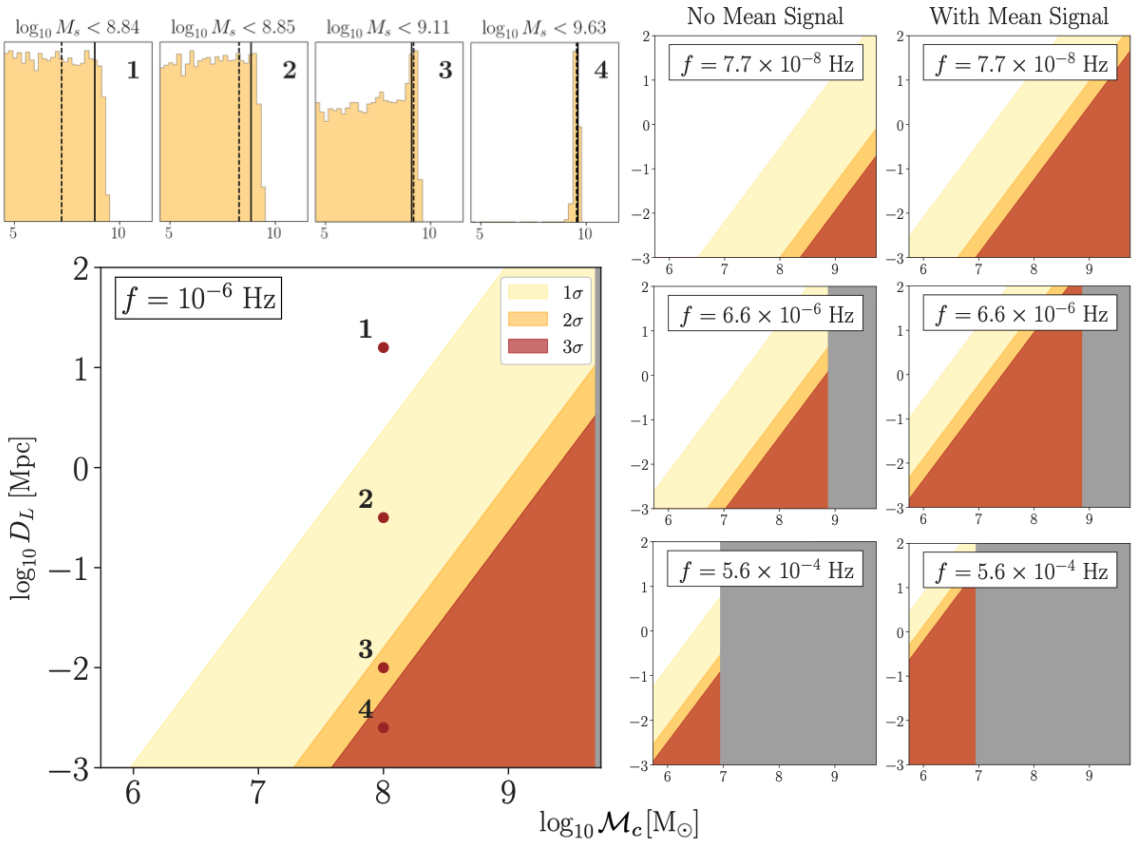

FIG. 4. Detection sensitivity of the Roman EML Survey in $\log_{10} \mathcal{M}_c - \log_{10} D_L$ space at multiple fixed frequency. Colors indicate detection thresholds at different confidence levels. *Top Left Panel:* Example posterior distributions for the scaled mass, $\log_{10} M_s$, corresponding to the chirp masses and distances indicated by the red points in the bottom left panel are shown in the top panels. Solid vertical lines on these figures show the upper bound of 90% confidence level. Dashed lines mark the injected signals. *Bottom Left Plot:* Sensitivity plotted in $\log_{10} \mathcal{M}_c - \log_{10} D_L$ space at 10^{-6} Hz with mean-subtracted signal. *Middle Column:* Sensitivity thresholds with mean-subtracted signals at different frequencies. *Right Column:* Sensitivity thresholds with full signal at different frequencies. In all panels, GW sources that reach the ISCO at the specified frequency or lower are blocked out in gray.

available in external catalogs, e.g., in the *Gaia* catalog [23]. Their astrometric solution in the Roman Space Telescope operational epoch is extrapolated from the external catalog measurement [a similar procedure to study proper motions of galactic bulge stars is described in 35]. The absolute astrometry of all stars in the FoV is then obtained in post-processing by simultaneously fitting the GSs to their extrapolated positions.

As argued in Section III, this tracking process will likely absorb a mean displacement signal within the FoV. Specifically for the Roman Space Telescope, this will be the mean deflections of the GSs. Though the choice of GSs is not yet available, we can gauge the effect of GS selection by repeating the MCMC study but subtracting only the mean of the GSs. For sim-

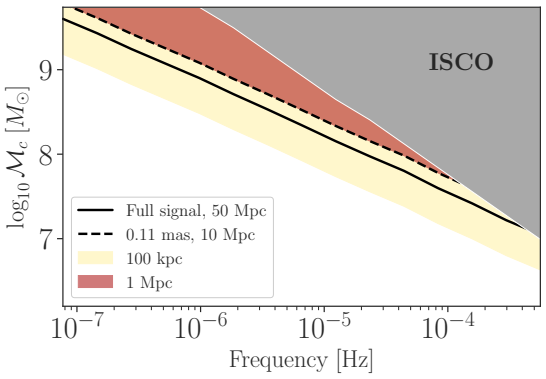

FIG. 5. Sensitivity of the Roman EML Survey to $\log_{10}\mathcal{M}_c$. The upper right corner (shaded gray) excludes massive systems that reach the ISCO at each frequency or lower. Detection sensitivity threshold is represented by the detectable chirp mass at a 2σ confidence level at various luminosity distances. Yellow and red blocks show detectable mass ranges at 1 Mpc and 100 kpc respectively, assuming the mean astrometric deflection is subtracted from the signal. The solid line shows the detection threshold at 10 Mpc if the astrometric accuracy were to improve to 0.11 mas, equivalent to a factor of 10 improvement in the sensitivity. The dashed line shows the sensitivity at 50 Mpc if the mean signal were observable, equivalent to a factor of 100 sensitivity improvement. See Section IV for further discussions.

plicity, we study two cases with 4 and 16 GSs. In each case, we model the detectors as square blocks that completely fill the FoV (i.e. no gaps, etc.) and place one GS in each of the square blocks. The position of the GS within each detector is then randomly chosen. We find that different GS choices only lead to $< 1\%$ variation in the upper limit confidence value, and having fewer GSs gives larger variations. Thus, our strategy to subtract the mean of all stars serves as a good reference regardless of the mission specifics.

This mean-subtraction process significantly reduces the effective signal, and the sensitivity level is generally two orders of magnitude lower than the full-signal scenario. Figure 5 shows that the Roman EML survey is most sensitive to very massive binaries $(\sim 10^8\ M_\odot)$ at close distances $(\sim 1$ Mpc). Since this is physically unlikely, the Roman EML survey with its current design will be limited as a GW probe.

This prediction is different from that for *Gaia* in [19], since a full-signal analysis is assumed. In the case of *Gaia*, this treatment is warranted since *Gaia* simultaneously observes through two widely separated FoVs and does not need to perform mean subtraction [26]. The sampled GW deflection patterns are consequently distinct and cannot be absorbed by the same pointing calibration process. For essentially the same reason, *Gaia* can measure absolute parallax rather than relative parallax [36].

While this outlined strategy is specific to the Roman EML survey, we note that the loss of the mean astrometric deflection signal is a typical feature of photometric surveys. Even though this loss presents a challenge for resolving individual GWs, the sensitivity might be better for joint signals of several GWs. We expect the combined GWs to produce a deflection pattern richer in features, and thus easier to detect. Such signals would come from SMBHBs at the centers of galaxies in the local universe, and the astrometric measurements can be used to study their population statistics. This is analogous to using PTA measurements to constrain the energy density of the stochastic GW background produced by massive black hole mergers across all redshifts [see, e.g., 17, 37, 38]. It is estimated that $\sim$ 100 continuous GW sources in the PTA band exist within 225 Mpc [39]. We may then speculate that a significant number of SMBHBs within our frequency range exist in the local universe, and their joint signal may be above detection threshold for the astrometry method.

B. Optimizing Photometric Surveys for GW

In this section, we give specific recommendations to maximize the GW detection potential of photometric surveys within the GW frequency gap of existing detection methods. We use the

expected performance of the Roman EML survey as a reference point and quantitatively describe a model survey capable of detecting a fiducial target, a $10^7\ M_\odot$ binary at 50 Mpc.

To estimate the required sensitivity, we proceed directly from Figure 5; the detection threshold is lowered by the same order of magnitude as the increase in effective signal strength. Therefore, to claim a 2σ detection on GWs from this new fiducial target, the model survey is 100 times more sensitive than the Roman EML survey. In the following sections we discuss ways to achieve this sensitivity.

1. *Mean-signal Recovery Fraction*

As suggested by the previous subsection, pointing reconstruction strategies determine whether the mean astrometric deflection could be observable, which translates into approximately two orders of magnitude sensitivity difference. Though the mean-subtracted deflection pattern and the full signal pattern differ in both the deflection magnitude averaged over all stars within the FoV and the pattern shape, we only use the average deflection magnitude as an approximate metric to compare sensitivity.

For our model FoV configuration, the average deflection magnitude after subtracting the mean is roughly 100 times smaller than the average full signal (see, for example, Figure 1), thus the sensitivity is roughly 100 times worse. We may then define a mean-signal recovery fraction to roughly quantify the observable deflection relative to the full signal. For example, a mean-signal recovery fraction of 50% implies that the average magnitude of the observable deflections after the astrometry solution is half of the full signal magnitude. Consequently, the sensitivity would be roughly 50 times higher than what we obtained from the MCMC study assuming mean-subtracted signals. Ideally, the photometric survey retains nearly all of the mean signal, relaxing the detection threshold by roughly a factor of 100. Such a model survey, with all other parameters similar to the Roman EML survey, can already detect the fiducial GW source. In general, higher recovery fraction allows detection of intrinsically weaker GW sources, such as farther and lighter systems, or the same system but much earlier in its evolution track.

2. *Astrometric Accuracy*

As shown by Equation 9, the strain amplitude threshold is linearly proportional to the astrometric accuracy. All else equivalent, the model survey improves upon the Roman Space Telescope accuracy by at least a factor of 100, giving a single-exposure single-source astrometric resolution better than 11 μas. In this work, we assume an astrometric accuracy of 1.1 mas, which is 1/100th of the detector pixel size [23]. We expect this accuracy to be routinely performed, but it is possible that 0.11 mas can be achieved [40]. In this case, the Roman EML survey will be ten times more sensitive and will already be able to detect binaries with $\mathcal{M}_c > 10^{7.6} M_\odot$ within 10 Mpc (see Figure 5).

For comparison, the astrometric accuracy of *Gaia* is $0.1 \sim 2$ mas (for $G = 17$ and $G = 21$ stars, respectively) [27]. The expected imaging resolution of the Square Kilometer Array (SKA)[2] [41] at 12.5 GHz is 0.04 arcsec [42]; assuming a fractional position error requirement smaller than 1% [43], the SKA can achieve an astrometric accuracy better than 0.4 mas.

3. *Number of Stars*

The statistical advantage of observing more stars ($\propto \sqrt{N_s}$) is stated in Equation 9. This number can be expressed as

$$\begin{aligned} N_s &= \int \alpha\left(\vec{r}\right) \rho\left(L, \vec{r}\right) dL\ d^3\vec{r}_{\rm obs} \\ &\approx A \int \alpha(\theta_0, \phi_0, r) \rho(L, \theta_0, \phi_0, r) r^2 dL\ dr\ , \end{aligned} \tag{24}$$

[2] https://www.skatelescope.org/the-ska-project/

where $\alpha(\vec{r})$ is the effective detectable fraction after photon loss during propagation (e.g., dust absorption, crowding effect, etc.), and $\rho(L, \vec{r})$ is the population density of luminosity-L stars. A is the covered angular area. In the second equality, we assume small variation of the integrand in the angular directions. Since GW detection requires frequent visit to the same field, we assume a "deep survey" mode where the total surveyed angular area is small and this equality is satisfied.

Evidently, the observational efficiency of telescopes is greatly increased if they can penetrate to further distances per area (i.e., large α). Therefore, a telescope with near-infrared filters outperforms one operating in the visible band, as near-infrared photons suffer less absorption by galactic dust along propagation. The optimal choice for the filter wavelength should, however, be balanced between this low-absorption advantage and the large-diffraction effect for long wavelengths, which degrades the point spread function and thus the astrometric accuracy.

The θ_0, ϕ_0 dependence suggests the importance of pointing directions. Specifically, surveys pointing toward the galactic center have larger ρ for fixed distance and luminosity. For magnitude limited surveys, this implies a larger number of observed stars. Conversely, surveys in high latitude regions are less advantageous since they observe fewer stars above certain magnitude limits. For comparison, the stellar density down to $H(AB) = 20$ mag at Galactic Latitude of 60 deg is approximately 3000 stars/deg^2 [44].

It is also intuitive that a larger FoV leads to more observed stars, all else equivalent. Therefore, the model survey will have comparable bands and pointing directions to the Roman Space Telescope during its EML survey, but with a 100 times larger ($\sim 200\,\mathrm{deg}^2$) survey area.

4. *FoV Size*

The effect of increasing the FoV size is partially degenerate with increasing the survey area, but it also allows for a larger deflection residual after mean subtraction. Specifically, the subtracted mean decreases as the variation across the FoV at each exposure becomes more significant. The combination of changes both in signal magnitude and pattern will likely be a complex effect that, in general, enhance the sensitivity. In principle, FoV patches can be stitched together to provide a larger effective FoV to include more pattern variation. However, the field-switching process must be exquisitely controlled such that the absorbed mean for each field is approximately the global mean solution in the larger effective FoV. However, due to the very large scale over which the GW-induced deflection pattern varies (on the order of tens of degrees), it is unlikely that future surveys can outperform the Roman EML survey by a factor of 100 through this means alone.

5. *Observational Cadence & Mission Length*

The impact of observational cadence is twofold: it determines the sensitive frequency range and contributes to the statistical improvement of sensitivity. To complement LISA, therefore, the upper limit frequency should be at least $\sim 10^{-5}$ Hz. It follows that an the model survey observes the same patch of sky at least once a day. For sensitivity improvement, the model survey has a longer effective observational time than the six 72-day epochs of the Roman EML survey. For example, a 10-year survey with full duty cycle improves the sensitivity by a factor of 3.

C. Other Potential Photometric GW Probes

In this section, we further develop the guidelines for assessing photometric surveys as GW

probes. We discuss ground-based and space-based telescopes in turn by pointing out their respective merits and drawbacks as potential GW probes. To the best of our knowledge, all the observatories discussed below would suffer from the limiting mean signal subtraction we discussed above.

A challenge with ground-based telescopes as GW probes lies in their relatively coarse astrometric resolution compared with space telescopes, due to atmospheric perturbation to the signal. For example, the Rubin Observatory[3] has a single-exposure astrometric accuracy of $\sim$ 11 mas [45], an order of magnitude larger than that of the Roman Space Telescope.

This resolution drawback can be partially compensated by a large number of observed stars, large FoV, and great observational flexibility. For instance, the Rubin Observatory is expected to observe a total of $\sim 4 \times 10^9$ stars with a FoV size of $\sim 10\,\mathrm{deg}^2$. Each sky patch is visited $\sim$ 100 times during its 10-year lifetime. By increasing its observational cadence by a factor of 5 ($\sim 1\ \mathrm{week}^{-1}$ on average), the Rubin Observatory would become sensitive to GWs with $f < 1.5 \times 10^{-6}$ Hz.

This astrometric method can also be applied to high-resolution radio telescopes, such as the SKA and the Next Generation Very Large Array (ngVLA)[4] [46]. As discussed, SKA can achieve an astrometric accuracy better than 0.4 mas. The ngVLA features a maximum baseline resolution as small as 0.17 mas at 41 GHz. It is also estimated that a large number of quasars can be observed in the radio band [see, e.g., $\sim 10^6$ in 47], which can serve as GW detectors instead of stars. Taking the SKA as an example, the relatively smaller number of observed quasars compared with stars observed by *Gaia* can potentially be compensated by a more frequent observation schedule to give similar performance at a higher frequency. Increasing the exposure time would also directly increase the number of detected quasars. Specifically, an SKA survey taking measurements every 40 minutes has a GW frequency band similar to that of the Roman EML survey ($f < 2 \times 10^{-4}$ Hz). To the authors' knowledge, there is currently no high-cadence survey planned.

Free from atmospheric effects, space-based telescopes can potentially observe a great number of stars to excellent precision. As an example, the ESA mission Euclid[5] is equipped with a near-infrared photometer with a ~ 1 mas single-exposure astrometric accuracy [48], similar to the expected performance of the Roman Space Telescope. The HabEx Workhorse Camera (HWC) onboard the Habitable Exoplanet Observatory (HabEx)[6] is expected to have similar, if not better, angular resolution to the Roman Space Telescope, albeit with a much smaller FoV [49].

The deciding factors then become the observed fields and observational cadence. Unlike the Roman Space Telescope, HabEx is not designed as a survey instrument; instead, it focuses on characterizing a handful of targets in great detail, and thus will not be suitable for our purpose. While Euclid does feature a deep survey, with $40\,\mathrm{deg}^2$ of sky observed every 15 days [48], these fields are close to the ecliptic pole with low stellar density. However, a high-cadence survey in its extended mission lifetime, following the recommendations we outline, could contribute meaningfully to GW detection.

V. CONCLUDING REMARKS

In this paper, we show how to use a photometric survey as a GW probe that uniquely bridges the GW frequency spectrum gap between existing detection methods. We discuss key factors that determine sensitivity. We then assess the potential of the Roman EML survey in its current definition as a GW probe. In Sec-

[3] https://www.lsst.org/lsst/
[4] https://ngvla.nrao.edu/
[5] https://sci.esa.int/web/euclid/home
[6] https://www.jpl.nasa.gov/habex/

tion IV, we make recommendations for maximizing the GW scientific output of photometric surveys and quantify the desirable performance via a model survey. Finally, we review existing and planned photometric surveys, and discuss their relative strengths and drawbacks as potential GW probes.

We note that our analysis can be refined in several ways. For instance, we have yet to explicitly include stellar proper motion in our simulation, which can in theory be subtracted via quadratic fitting. Such proper motions may even be correlated across the FoV, if, for example, open clusters are present. However, we expect these motions to have limited impact on the GW sensitivity once we consider the signal variation over time. Especially for high-frequency GWs, their oscillatory nature leaves a distinct signature from physical proper motion over long timescales.

We could also model the seven fields of the Roman EML survey jointly. A combined analysis of the data from all fields might amount to having a larger effective FoV, should the temporal and pointing accuracy during the field-switching process allow. Incorporating the GW frequency evolution could also enhance sensitivity.

The recommendations in Section III should serve as a reference for maximizing GW science from future photometric surveys. The current expected performance of the Roman Space Telescope could make detecting individual GWs a challenge. However, with some luck and a novel pointing reconstruction strategy, we may yet detect individual GWs with the Roman Space Telescope.

ACKNOWLEDGMENTS

We are deeply grateful for discussions with Jeff Kruk, Scott Gaudi, and Davy Kirkpatric on the Roman Space Telescope, as well as Robert Lupton on the Rubin Observatory and Joseph Lazio and Steven Myers on the ngVLA. We thank Todd Gaier for a discussion that inspired this work. YW would like to thank the David and Ellen Lee Distinguished Fellowship for support during this research. Part of this work was done at Jet Propulsion Laboratory, California Institute of Technology, under a contract with the National Aeronautics and Space Administration. This work was supported by NASA grant 15-WFIRST15-0008 *Cosmology with the High Latitude Survey* Roman Science Investigation Team (SIT).

Software: astropy [50], astroquery [51], emcee [52], matplotlib [53], numpy [54], scipy [55]

[1] The LIGO Scientific Collaborationand the Virgo Collaboration, arXiv e-prints , arXiv:2004.08342 (2020), arXiv:2004.08342 [astro-ph.HE].

[2] B. P. Abbott *et al.* (LIGO Scientific Collaboration and Virgo Collaboration), Phys. Rev. Lett. **119**, 161101 (2017), arXiv:1710.05832 [gr-qc].

[3] J. Aasi *et al.* (LIGO Scientific Collaboration), Classical and Quantum Gravity **32**, 074001 (2015), arXiv:1411.4547 [gr-qc].

[4] K. A. Kuns, H. Yu, Y. Chen, and R. X. Adhikari, arXiv e-prints , arXiv:1908.06004 (2019), arXiv:1908.06004 [gr-qc].

[5] S. Kawamura, T. Nakamura, M. Ando, N. Seto, T. Akutsu, *et al.*, International Journal of Modern Physics D **28**, 1845001 (2019).

[6] P. Amaro-Seoane, H. Audley, S. Babak, J. Baker, E. Barausse, *et al.*, arXiv e-prints , arXiv:1702.00786 (2017), arXiv:1702.00786 [astro-ph.IM].

[7] J. Luo, L.-S. Chen, H.-Z. Duan, Y.-G. Gong, S. Hu, J. Ji, Q. Liu, J. Mei, V. Milyukov, M. Sazhin, C.-G. Shao, V. T. Toth, H.-B. Tu, Y. Wang, Y. Wang, H.-C. Yeh, M.-S. Zhan, Y. Zhang, V. Zharov, and Z.-B. Zhou, Classical and Quantum Gravity **33**, 035010 (2016), arXiv:1512.02076 [astro-ph.IM].

[8] L. Science Instrument List, :, A. Buikema, C. Cahillane, G. L. Mansell, C. D. Blair, R. Abbott, C. Adams, R. X. Adhikari, A. Ananyeva, S. Appert, K. Arai, J. S. Areeda, Y. Asali, S. M. Aston, C. Austin, A. M. Baer, M. Ball,

S. W. Ballmer, S. Banagiri, D. Barker, L. Barsotti, J. Bartlett, B. K. Berger, J. Betzwieser, D. Bhattacharjee, G. Billingsley, S. Biscans, *et al.*, arXiv e-prints , arXiv:2008.01301 (2020), arXiv:2008.01301 [astro-ph.IM].

[9] J. I. Thorpe, J. Ziemer, I. Thorpe, J. Livas, J. W. Conklin, R. Caldwell, E. Berti, S. T. McWilliams, R. Stebbins, D. Shoemaker, E. C. Ferrara, S. L. Larson, *et al.*, in BAAS, Vol. 51 (2019) p. 77.

[10] C. J. Moore, S. R. Taylor, and J. R. Gair, Classical and Quantum Gravity **32**, 055004 (2015), arXiv:1406.5199 [astro-ph.IM].

[11] S. Babakand A. Sesana, Phys. Rev. D **85**, 044034 (2012), arXiv:1112.1075 [astro-ph.CO].

[12] J. A. Ellis, X. Siemens, and J. D. E. Creighton, ApJ **756**, 175 (2012), arXiv:1204.4218 [astro-ph.IM].

[13] S. R. Taylor, M. Vallisneri, J. A. Ellis, C. M. F. Mingarelli, T. J. W. Lazio, and R. van Haasteren, ApJ **819**, L6 (2016), arXiv:1511.05564 [astro-ph.IM].

[14] J. P. W. Verbiest, L. Lentati, G. Hobbs, R. van Haasteren, P. B. Demorest, *et al.*, MNRAS **458**, 1267 (2016), arXiv:1602.03640 [astro-ph.IM].

[15] A. Sesana, A. Vecchio, and C. N. Colacino, MNRAS **390**, 192 (2008), arXiv:0804.4476 [astro-ph].

[16] L. G. Bookand É. É. Flanagan, Phys. Rev. D **83**, 024024 (2011), arXiv:1009.4192 [astro-ph.CO].

[17] T. Pyne, C. R. Gwinn, M. Birkinshaw, T. M. Eubanks, and D. N. Matsakis, ApJ **465**, 566 (1996), arXiv:astro-ph/9507030 [astro-ph].

[18] S. A. Klioner, Classical and Quantum Gravity **35**, 045005 (2018), arXiv:1710.11474 [astro-ph.HE].

[19] C. J. Moore, D. P. Mihaylov, A. Lasenby, and G. Gilmore, Phys. Rev. Lett. **119**, 261102 (2017), arXiv:1707.06239 [astro-ph.IM].

[20] A. Agrawal, T. Okumura, and T. Futamase, Phys. Rev. D **100**, 063534 (2019), arXiv:1907.02328 [astro-ph.CO].

[21] Roman's Key Science Components (2020).

[22] B. S. Gaudi, R. Akeson, J. Anderson, E. Bachelet, D. P. Bennett, A. Bhattacharya, V. Bozza, S. Calchi Novati, C. B. Henderson, S. A. Johnson, J. Kruk, J. R. Lu, S. Mao, B. T. Montet, D. M. Nataf, M. T. Penny, R. Poleski, C. Ranc, K. Sahu, Y. Shvartzvald, D. N. Spergel, D. Suzuki, K. G. Stassun, and R. A. Street, BAAS **51**, 211 (2019), arXiv:1903.08986 [astro-ph.SR].

[23] WFIRST Astrometry Working Group, R. E. Sanderson, A. Bellini, S. Casertano, J. R. Lu, P. Melchior, M. Libralato, D. Bennett, M. Shao, J. Rhodes, S. T. Sohn, S. Malhotra, S. Gaudi, S. M. Fall, E. Nelan, P. Guhathakurta, J. Anderson, and S. Ho, Journal of Astronomical Telescopes, Instruments, and Systems **5**, 044005 (2019).

[24] M. Anholm, S. Ballmer, J. D. E. Creighton, L. R. Price, and X. Siemens, Phys. Rev. D **79**, 084030 (2009), arXiv:0809.0701 [gr-qc].

[25] L. Blanchet, Living Reviews in Relativity **17**, 2 (2014), arXiv:1310.1528 [gr-qc].

[26] T. Prusti *et al.* (Gaia Collaboration), A&A **595**, A1 (2016), arXiv:1609.04153 [astro-ph.IM].

[27] A. G. A. Brown *et al.* (Gaia Collaboration), A&A **616**, A1 (2018), arXiv:1804.09365 [astro-ph.GA].

[28] C. J. Moore, R. H. Cole, and C. P. L. Berry, Classical and Quantum Gravity **32**, 015014 (2015), arXiv:1408.0740 [gr-qc].

[29] E. S. Phinney, arXiv e-prints , astro-ph/0108028 (2001), arXiv:astro-ph/0108028 [astro-ph].

[30] L. E. Kidder, Phys. Rev. D **52**, 821 (1995), arXiv:gr-qc/9506022 [gr-qc].

[31] X. Luri, A. G. A. Brown, L. M. Sarro, F. Arenou, C. A. L. Bailer-Jones, A. Castro-Ginard, J. de Bruijne, T. Prusti, C. Babusiaux, and H. E. Delgado, A&A **616**, A9 (2018), arXiv:1804.09376 [astro-ph.IM].

[32] T. Robson, N. J. Cornish, and C. Liu, Classical and Quantum Gravity **36**, 105011 (2019), arXiv:1803.01944 [astro-ph.HE].

[33] C. Cutlerand É. E. Flanagan, Phys. Rev. D **49**, 2658 (1994), arXiv:gr-qc/9402014 [gr-qc].

[34] A. Sesana, F. Haardt, P. Madau, and M. Volonteri, ApJ **611**, 623 (2004), arXiv:astro-ph/0401543 [astro-ph].

[35] W. Clarkson, K. Sahu, J. Anderson, T. E. Smith, T. M. Brown, R. M. Rich, S. Casertano, H. E. Bond, M. Livio, D. Minniti, N. Panagia, A. Renzini, J. Valenti, and M. Zoccali, ApJ **684**, 1110 (2008), arXiv:0809.1682 [astro-ph].

[36] L. Lindegrenand U. Bastian, in *EAS Publications Series*, EAS Publications Series, Vol. 45 (2010) pp. 109–114.

[37] R. van Haasteren, Y. Levin, G. H. Janssen, K. Lazaridis, M. Kramer, B. W. Stappers, G. Desvignes, M. B. Purver, A. G. Lyne, R. D. Ferdman, A. Jessner, I. Cognard, G. Theureau,

N. D'Amico, A. Possenti, M. Burgay, A. Corongiu, J. W. T. Hessels, R. Smits, and J. P. W. Verbiest, MNRAS **414**, 3117 (2011), arXiv:1103.0576 [astro-ph.CO].

[38] Z. Arzoumanian, P. T. Baker, A. Brazier, S. Burke-Spolaor, S. J. Chamberlin, S. Chatterjee, B. Christy, J. M. Cordes, N. J. Cornish, F. Crawford, H. Thankful Cromartie, K. Crowter, M. DeCesar, P. B. Demorest, T. Dolch, J. A. Ellis, others, and NANOGrav Collaboration, ApJ **859**, 47 (2018), arXiv:1801.02617 [astro-ph.HE].

[39] C. M. F. Mingarelli, T. J. W. Lazio, A. Sesana, J. E. Greene, J. A. Ellis, C.-P. Ma, S. Croft, S. Burke-Spolaor, and S. R. Taylor, Nature Astronomy **1**, 886 (2017), arXiv:1708.03491 [astro-ph.GA].

[40] J. Kruk, personal communication.

[41] A. Weltman, P. Bull, S. Camera, K. Kelley, H. Padmanabhan, J. Pritchard, A. Raccanelli, S. Riemer-Sørensen, L. Shao, S. Andrianomena, E. Athanassoula, D. Bacon, R. Barkana, G. Bertone, C. Bœhm, C. Bonvin, A. Bosma, M. Brüggen, *et al.*, PASA **37**, e002 (2020), arXiv:1810.02680 [astro-ph.CO].

[42] Technical Information - the Telescopes (2018).

[43] *SKA1 level 0 science requirements*, Tech. Rep. SKA-TEL-SKO-0000007 (2015).

[44] Y. Mellier, in *Science from the Next Generation Imaging and Spectroscopic Surveys* (2012) p. 3.

[45] Ž. Ivezić, S. M. Kahn, J. A. Tyson, B. Abel, E. Acosta, R. Allsman, D. Alonso, Y. AlSayyad, S. F. Anderson, J. Andrew, J. R. P. Angel, G. Z. Angeli, R. Ansari, P. Antilogus, C. Araujo, R. Armstrong, K. T. Arndt, P. Astier, *et al.*, ApJ **873**, 111 (2019), arXiv:0805.2366 [astro-ph].

[46] M. McKinnon, A. Beasley, E. Murphy, R. Selina, R. Farnsworth, and A. Walter, in BAAS, Vol. 51 (2019) p. 81.

[47] A. H. Jaffe, New A Rev. **48**, 1483 (2004), arXiv:astro-ph/0409637 [astro-ph].

[48] W. Percival, M. Balogh, D. Bond, J. Bovy, R. Carlberg, S. Chapman, P. Cote, N. Cowan, S. Fabbro, L. Ferrarese, S. Gwyn, R. Hlozek, M. Hudson, J. Hutchings, J. Kavelaars, D. Lang, A. McConnachie, A. Muzzin, L. Parker, C. Pritchet, M. Sawicki, D. Schade, D. Scott, K. Smith, K. Spekkens, J. Taylor, and C. Willott, in *Canadian Long Range Plan for Astronony and Astrophysics White Papers*, Vol. 2020 (2019) p. 20.

[49] B. S. Gaudi, S. Seager, B. Mennesson, A. Kiessling, K. Warfield, K. Cahoy, J. T. Clarke, S. Domagal-Goldman, L. Feinberg, O. Guyon, J. Kasdin, D. Mawet, P. Plavchan, T. Robinson, L. Rogers, P. Scowen, *et al.*, arXiv e-prints , arXiv:2001.06683 (2020), arXiv:2001.06683 [astro-ph.IM].

[50] Astropy Collaboration, A. M. Price-Whelan, B. M. Sipőcz, H. M. Günther, P. L. Lim, S. M. Crawford, S. Conseil, D. L. Shupe, M. W. Craig, N. Dencheva, A. Ginsburg, J. T. Vand erPlas, L. D. Bradley, D. Pérez-Suárez, M. de Val-Borro, T. L. Aldcroft, K. L. Cruz, T. P. Robitaille, E. J. Tollerud, C. Ardelean, T. Babej, others, and Astropy Contributors, AJ **156**, 123 (2018), arXiv:1801.02634 [astro-ph.IM].

[51] A. Ginsburg, B. M. Sipőcz, C. E. Brasseur, P. S. Cowperthwaite, M. W. Craig, C. Deil, J. Guillochon, G. Guzman, S. Liedtke, P. Lian Lim, K. E. Lockhart, M. Mommert, B. M. Morris, H. Norman, M. Parikh, M. V. Persson, T. P. Robitaille, J.-C. Segovia, L. P. Singer, E. J. Tollerud, M. de Val-Borro, I. Valtchanov, J. Woillez, Astroquery Collaboration, and a subset of astropy Collaboration, AJ **157**, 98 (2019), arXiv:1901.04520 [astro-ph.IM].

[52] D. Foreman-Mackey, A. Conley, W. Meierjurgen Farr, D. W. Hogg, D. Lang, P. Marshall, A. Price-Whelan, J. Sanders, and J. Zuntz, emcee: The MCMC Hammer (2013), ascl:1303.002.

[53] J. D. Hunter, Computing in Science and Engineering **9**, 90 (2007).

[54] S. van der Walt, S. C. Colbert, and G. Varoquaux, Computing in Science and Engineering **13**, 22 (2011), arXiv:1102.1523 [cs.MS].

[55] P. Virtanen, R. Gommers, T. E. Oliphant, M. Haberland, T. Reddy, D. Cournapeau, E. Burovski, P. Peterson, W. Weckesser, J. Bright, S. J. van der Walt, M. Brett, J. Wilson, K. Jarrod Millman, N. Mayorov, A. R. J. Nelson, E. Jones, R. Kern, E. Larson, C. Carey, İ. Polat, Y. Feng, E. W. Moore, J. Vand erPlas, D. Laxalde, J. Perktold, R. Cimrman, I. Henriksen, E. A. Quintero, C. R. Harris, A. M. Archibald, A. H. Ribeiro, F. Pedregosa, P. van Mulbregt, and S. . . Contributors, Nature Methods **17**, 261 (2020).